Journal of Sound and Vibration 327 (2009) 9–25

Contents lists available at ScienceDirect

Journal of Sound and Vibration

journal homepage: www.elsevier.com/locate/jsvi

An electromechanical finite element model for piezoelectric energy harvester plates

Carlos De Marqui Junior [a,*], Alper Erturk [b], Daniel J. Inman [c]

[a] Department of Aeronautical Engineering, Engineering School of Sao Carlos, University of Sao Paulo, Brazil
[b] Center for Intelligent Material Systems and Structures, Department of Engineering Science and Mechanics, Virginia Tech, USA
[c] Center for Intelligent Material Systems and Structures, Department of Mechanical Engineering, Virginia Tech, USA

ARTICLE INFO

Article history:
Received 13 January 2009
Received in revised form
5 May 2009
Accepted 12 May 2009
Handling Editor: C.L. Morfey
Available online 11 June 2009

ABSTRACT

Vibration-based energy harvesting has been investigated by several researchers over the last decade. The goal in this research field is to power small electronic components by converting the waste vibration energy available in their environment into electrical energy. Recent literature shows that piezoelectric transduction has received the most attention for vibration-to-electricity conversion. In practice, cantilevered beams and plates with piezoceramic layers are employed as piezoelectric energy harvesters. The existing piezoelectric energy harvester models are beam-type lumped parameter, approximate distributed parameter and analytical distributed parameter solutions. However, aspect ratios of piezoelectric energy harvesters in several cases are plate-like and predicting the power output to general (symmetric and asymmetric) excitations requires a plate-type formulation which has not been covered in the energy harvesting literature. In this paper, an electromechanically coupled finite element (FE) plate model is presented for predicting the electrical power output of piezoelectric energy harvester plates. Generalized Hamilton's principle for electroelastic bodies is reviewed and the FE model is derived based on the Kirchhoff plate assumptions as typical piezoelectric energy harvesters are thin structures. Presence of conductive electrodes is taken into account in the FE model. The predictions of the FE model are verified against the analytical solution for a unimorph cantilever and then against the experimental and analytical results of a bimorph cantilever with a tip mass reported in the literature. Finally, an optimization problem is solved where the aluminum wing spar of an unmanned air vehicle (UAV) is modified to obtain a generator spar by embedding piezoceramics for the maximum electrical power without exceeding a prescribed mass addition limit.

1. Introduction

The research interest in converting ambient vibration energy to usable electrical energy has increased in the last years [1–5]. The concept of energy harvesting is particularly useful for wireless sensors powered by batteries and remotely operated systems with limited energy source. The goal of the research in vibration-based energy harvesting is to provide electrical energy for such systems by utilizing the vibrations available in their environment. Unmanned air vehicles (UAVs) and micro air vehicles (MAVs) constitute unique application systems where the possibility of an additional energy source is very important. UAVs are designed to maximize the endurance and flight range with the limited energy available in operation. A possible

* Corresponding author. Tel.: +55 16 33739417; fax: +55 16 33739590.
E-mail addresses: demarqui@sc.usp.br (C. De Marqui Junior), erturk@vt.edu (A. Erturk), dinman@vt.edu (D.J. Inman).

0022-460X/$ - see front matter © 2009 Elsevier Ltd. All rights reserved.
doi:10.1016/j.jsv.2009.05.015

source of energy for charging the batteries of UAVs is the mechanical vibration energy due to unsteady aerodynamic loads during the flight [6] and due to ground excitation in perching [7,8]. Different transduction mechanisms (piezoelectric [9–12], electromagnetic [13–17] and electrostatic [18,19]) can be used for converting vibrations to electricity. However, the recent literature shows that piezoelectric transduction has received the most attention for vibration-based energy harvesting and several review articles directly focusing on piezoelectric energy harvesting can be found in the literature [1,3–5].

Piezoelectric power generators can harvest electrical energy from mechanical vibrations based on the direct piezoelectric effect. These generators have been extensively studied as a low-cost and efficient alternative for low-level energy harvesting. Researchers have proposed various models to represent the electromechanical behavior of piezoelectric energy harvesters, which range from lumped parameter models [9,20] to Rayleigh–Ritz type approximate distributed parameter models [10,11,20] as well as analytical distributed parameter solution attempts [21,22]. Recently, certain issues observed in some of these lumped parameter and distributed parameter piezoelectric energy harvester models have been clarified in the literature [23]. More recently, the analytical distributed parameter solutions for unimorph [12,24] and bimorph [25] piezoelectric energy harvester configurations with closed-form expressions have been presented. Convergence of the Rayleigh–Ritz type electromechanical solution [10,11,20] to the analytical solution given by Erturk and Inman [24] was observed by Elvin and Elvin [26] when sufficient number of admissible functions were used. The lumped parameter solution [20] have been found useful for a fundamental understanding of the problem and to investigate the optimization of system parameters for better electrical outputs [27,28]. However, accurate prediction of the electromechanical behavior of piezoelectric energy harvesters requires using distributed parameter solutions. Experimental verifications and validations were also reported for the approximate [10,11] and analytical [12,25] (beam-type) distributed parameter electromechanical solutions.

The literature of piezoelectric sensing and actuation includes finite element (FE) models for plates with piezoceramic materials [29–33]. Although these FE models have not been used to study the energy harvesting problem, they provide the basis for modeling of a piezoelectric energy harvester. As far as the literature of FE modeling is considered, it can be observed that some of these FE models do not account for the presence of conductive electrodes bracketing the piezoceramic layer (e.g., [29]); although, in practice, piezoceramic layers usually come with highly conductive electrode layers from the manufacturer. If the presence of the conductive electrodes is not taken into consideration, a space-dependent electric potential distribution is obtained throughout the surface of the piezoceramic, yielding a different electric potential term (i.e., electrical degree of freedom) for each finite element. Some authors have considered the presence of the electrodes in the electromechanical problem [30,31] and obtained one voltage output (i.e., potential difference) between the electrode pair covering the piezoceramic. However, regardless of this electrode-based consideration, most of these models in the literature have focused on structural actuation and damping and plate-type formulation has not been considered in the literature of energy harvesting.

This work presents an electromechanical FE plate model for piezoelectric energy harvesting. Since piezoelectric energy harvesters are designed and manufactured as thin structures, the classical plate theory is employed in the formulation. A resistive electrical load is considered in the electrical domain, in agreement with the simplified analyses followed by others [9–12,20–26]. Electrical circuitry-based work dealing with AC-to-DC (alternating current-to-direct current) converters can be found in the literature [34–37]. First the FE model is verified against the analytical solution for a unimorph cantilever under base excitation presented by Erturk and Inman [24]. The electromechanical frequency response functions (FRFs) obtained using the FE model are compared with the analytically obtained FRFs referred from the aforementioned work. As a second case study, the analytical and experimental FRFs of a bimorph cantilever with a tip mass reported by Erturk and Inman [25] are predicted by using the FE model. Finally, the FE model is used to solve an optimization problem for UAV applications. The aluminum wing spar of a UAV is modified to design a generator wing spar. Since mass densities of typical piezoceramics are considerably large for UAV applications, a limiting value for mass addition is imposed to the problem as a design constraint. Dimensions of the embedded piezoceramic are identified for the maximum electrical power output of the generator spar with embedded piezoceramics.

2. Finite element modeling of a piezoelectric energy harvester plate

2.1. Generalized Hamilton's principle for a piezoelectric energy harvester

In the absence of magnetic effects, the generalized Hamilton's principle for an electroelastic body is [38]

$$\int_{t_1}^{t_2} [\delta(T - U + W_e) + \delta W]\,\mathrm{d}t = 0 \tag{1}$$

where the total kinetic energy (T), the total potential energy (U) and the electrical energy (W_e) terms are defined as

$$T = \int_{V_s} \frac{1}{2}\rho_s \dot{\mathbf{u}}^t \dot{\mathbf{u}}\,\mathrm{d}V_s + \int_{V_p} \frac{1}{2}\rho_p \dot{\mathbf{u}}^t \dot{\mathbf{u}}\,\mathrm{d}V_p \tag{2a}$$

$$U = \int_{V_s} \frac{1}{2}\mathbf{S}^t\mathbf{T}\,\mathrm{d}V_s + \int_{V_p} \frac{1}{2}\mathbf{S}^t\mathbf{T}\,\mathrm{d}V_p \tag{2b}$$

$$W_e = \int_{V_p} \frac{1}{2}\mathbf{E}^t\mathbf{D}\,dV_p \tag{2c}$$

Here, $\mathbf{u}$ is the vector of mechanical displacements, $\mathbf{S}$ is the vector of mechanical strain components, $\mathbf{T}$ is the vector of mechanical stress components, $\mathbf{D}$ is the vector of electric displacement components, $\mathbf{E}$ is the vector of electric field components, ρ is the mass density, V is the volume, t denotes transpose when it is used as a superscript (otherwise it stands for the time) and an over-dot represents differentiation with respect to time. Here and hereafter, subscripts s and p stand for the substructure and piezoceramic layers, respectively.

For a set of discrete mechanical forces $\mathbf{f}$ applied at locations (x_i, y_i) and for a set of discrete electric charge outputs q extracted at locations (x_j, y_j), one can express the variation of the *mechanically applied* and *electrically extracted* work as follows:

$$\delta W = \sum_{i=1}^{nf} \delta\mathbf{u}(x_i, y_i, t)\cdot\mathbf{f}(x_i, y_i, t) + \sum_{j=1}^{nq} \delta\varphi(x_j, y_j, t)q(x_j, y_j, t) \tag{3}$$

where nf is the number of discrete mechanical forces, φ_j is the scalar electrical potential and nq is the number of discrete electrode pairs.

The generalized Hamilton's principle for electroelastic bodies [38] described by the foregoing equations was previously employed by Hagood et al. [39] where they combined the Rayleigh–Ritz method and Euler–Bernoulli beam theory for active structural control. The Rayleigh–Ritz formulation given by Hagood et al. [39] was recently implemented by Sodano et al. [10] and duToit et al. [11,20] for predicting the electrical power output of cantilevered Euler–Bernoulli beams in energy harvesting. It should be mentioned that, as oppose to the energy harvesting problem, the electric charge is the input in the structural actuation problem, and therefore the second term in Eq. (3) has a minus sign in Hagood et al. [39]. Note that the energy dissipation due to mechanical damping is excluded at this point and it will be introduced later in the form of proportional damping.

The linear-elastic constitutive relation for the substructure material can be written as

$$\mathbf{T} = \mathbf{c}_s\mathbf{S} \tag{4a}$$

and the linear-electroelastic constitutive relation for the piezoceramic material is [40]

$$\begin{Bmatrix}\mathbf{T}\\ \mathbf{D}\end{Bmatrix} = \begin{bmatrix}\mathbf{c}_p^E & -\mathbf{e}^t\\ \mathbf{e} & \boldsymbol{\varepsilon}^S\end{bmatrix}\begin{Bmatrix}\mathbf{S}\\ \mathbf{E}\end{Bmatrix} \tag{4b}$$

where $\mathbf{c}$ is the elastic stiffness matrix, $\mathbf{e}$ is the matrix of piezoelectric constants, $\boldsymbol{\varepsilon}$ is the matrix of permittivity components, superscript E and S denote that the parameters are measured at constant electric field and constant strain, respectively.

Using the constitutive relations given by Eqs. (4a) and (4b) in Eq. (1), the generalized Hamilton's principle for a piezoelectric energy harvester becomes

$$\int_{t_1}^{t_2}\left[\int_{V_s}\rho_s\delta\dot{\mathbf{u}}^t\dot{\mathbf{u}}\,dV_s + \int_{V_p}\rho_p\delta\dot{\mathbf{u}}^t\dot{\mathbf{u}}\,dV_p - \int_{V_s}\delta\mathbf{S}^t\mathbf{c}_s\mathbf{S}\,dV_s - \int_{V_p}\delta\mathbf{S}^t\mathbf{c}_p^E\mathbf{S}\,dV_p + \int_{V_p}\delta\mathbf{S}^t\mathbf{e}^t\mathbf{E}\,dV_p + \int_{V_p}\delta\mathbf{E}^t\mathbf{e}\mathbf{S}\,dV_p + \int_{V_p}\delta\mathbf{E}^t\boldsymbol{\varepsilon}^S\mathbf{E}\,dV_p + \sum_{i=1}^{nf}\delta\mathbf{u}(x_i, y_i, t)\cdot\mathbf{f}(x_i, y_i, t) + \sum_{j=1}^{nq}\delta\varphi(x_j, y_j, t)q(x_j, y_j, t)\right]dt = 0 \tag{5}$$

2.2. Electromechanically coupled finite element model

The derivation given in the following is for a unimorph piezoelectric energy harvester configuration, i.e., the harvester plate has one substructure layer and one piezoceramic layer as shown in Fig. 1. However, the formulation can easily be extended to bimorph configurations (plates with two piezoceramic layers bracketing a substructure layer) as summarized at the end of this section. The substructure and the piezoceramic layers are assumed to be perfectly bonded to each other. The piezoceramic layer (which is poled in the thickness direction) is covered by continuous electrodes (which are assumed to be perfectly conductive) with negligible thickness. As a common practice in the literature [9–12,20–26], a resistive load is considered in the electrical domain and the purpose is to estimate the power generated in the electrical domain due to mechanical vibrations of the energy harvester plate. In general, as depicted in Fig. 1, piezoelectric energy harvesters are designed to have clamped-free (cantilevered) boundary conditions and the source of excitation is the vibratory motion of the clamped end. Since piezoelectric energy harvesters are manufactured as thin structures for improved flexibility, the classical (Kirchhoff) plate theory is employed in the formulation.

A rectangular finite element with three mechanical degrees of freedom per node (namely the displacements u, v and w in x, y and z directions) shown in Fig. 2 is used to model the substructure and the piezoceramic layers. Based on the assumption that each finite element of the piezoceramic layer is completely covered with perfectly conductive electrodes (on the top and the bottom surfaces), one electrical degree of freedom (voltage v_p across the electrodes) is sufficient for modeling the electrical response of these elements. Thus, the rectangular finite element in Fig. 2 has 13 degrees of freedom in total.

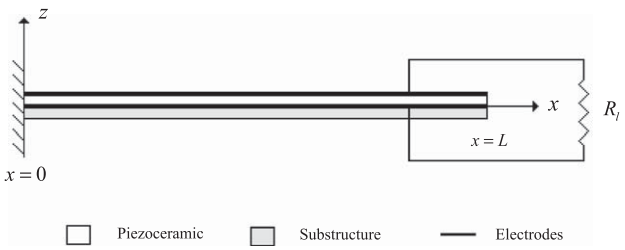

Fig. 1. A unimorph piezoelectric energy harvester plate with clamped-free boundary conditions.

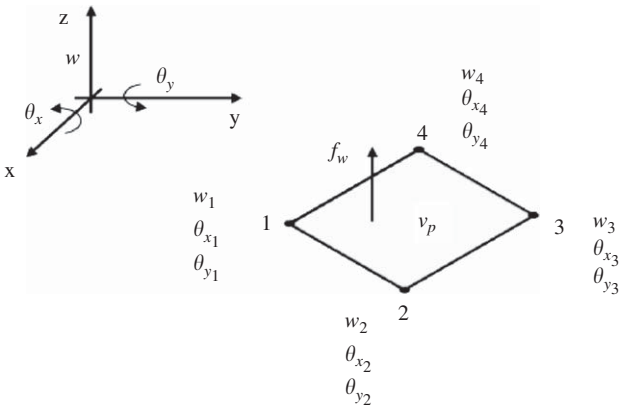

Fig. 2. Piezoelectric finite element with 12 mechanical degrees of freedom and 1 electrical degree of freedom.

Based on the Kirchhoff plate theory, transverse shear strains and rotary inertias of the finite elements are neglected and in-plane displacements (u and v) are assumed to be due to the bending (cross-section rotation) of the plate only. The displacement field is then

$$\begin{Bmatrix} u \\ v \\ w \end{Bmatrix} = \begin{Bmatrix} -z\dfrac{\partial w}{\partial x} & -z\dfrac{\partial w}{\partial y} & w \end{Bmatrix}^{\mathrm{t}} \tag{6}$$

where the displacement components u, v and w at a thickness level z from the reference (neutral) surface are given in terms of the transverse deflection (w) of the reference surface.

The mechanical strain components can be written in terms of the displacement components as

$$\begin{Bmatrix} S_x \\ S_y \\ 2S_{xy} \end{Bmatrix} = \begin{Bmatrix} \dfrac{\partial u}{\partial x} & \dfrac{\partial v}{\partial y} & \dfrac{\partial u}{\partial y}+\dfrac{\partial v}{\partial x} \end{Bmatrix}^{\mathrm{t}} = -z\begin{Bmatrix} \dfrac{\partial^2 w}{\partial x^2} & \dfrac{\partial^2 w}{\partial y^2} & 2\dfrac{\partial^2 w}{\partial x\,\partial y} \end{Bmatrix}^{\mathrm{t}} \tag{7}$$

The transverse displacement of node k of the rectangular finite element shown in Fig. 2 is assumed to vary in the polynomial form [41]

$$w_k = w|_{x_k,y_k} = \mathbf{P}|_{x_k,y_k}\boldsymbol{\mu} \tag{8a}$$

and consequently the bending rotations can be given as

$$\theta_{xk} = \left.\frac{\partial w}{\partial y}\right|_{x_k,y_k} = \left.\frac{\partial \mathbf{P}}{\partial y}\right|_{x_k,y_k}\boldsymbol{\mu} \tag{8b}$$

$$\theta_{yk} = -\left.\frac{\partial w}{\partial x}\right|_{x_k,y_k} = -\left.\frac{\partial \mathbf{P}}{\partial x}\right|_{x_k,y_k}\boldsymbol{\mu} \tag{8c}$$

where the polynomial terms are

$$\mathbf{P} = [1 \;\; x \;\; y \;\; x^2 \;\; xy \;\; y^2 \;\; x^3 \;\; x^2y \;\; xy^2 \;\; y^3 \;\; x^3y \;\; xy^3] \tag{9}$$

and the vector of generalized coordinates is

$$\boldsymbol{\mu} = [a_1 \;\; a_2 \;\; a_3 \;\; a_4 \;\; a_5 \;\; a_6 \;\; a_7 \;\; a_8 \;\; a_9 \;\; a_{10} \;\; a_{11} \;\; a_{12}]^{\mathrm{t}} \tag{10}$$

Considering the 4 nodes per element and the 3 degrees of freedom per node, one can define the 12×1 vector of nodal variables as

$$\boldsymbol{\psi} = \{w_1 \;\; \theta_{x1} \;\; \theta_{y1} \;\; w_2 \;\; \theta_{x2} \;\; \theta_{y2} \;\; w_3 \;\; \theta_{x3} \;\; \theta_{y3} \;\; w_4 \;\; \theta_{x4} \;\; \theta_{y4}\}^{\mathrm{t}} \tag{11}$$

which can be expressed in the form of

$$\boldsymbol{\psi} = \mathbf{A}\boldsymbol{\mu} \tag{12}$$

where $\mathbf{A}$ is a 12×12 transformation matrix [41] whose elements are given by $\mathbf{P}$ and its derivatives through the definitions of w_k, θ_{xk} and θ_{yk} given by Eqs. (8a)–(8c).

Nodal approximations for the transverse deflection as functions of the nodal variables are then

$$w \cong w_k = \boldsymbol{\Gamma}\boldsymbol{\psi} \tag{13}$$

where

$$\boldsymbol{\Gamma} = \mathbf{P}\mathbf{A}^{-1} \tag{14}$$

The vector of transverse displacement and cross-section rotations is related to the vector of nodal variables as follows:

$$\left\{ \frac{\partial w}{\partial x} \quad \frac{\partial w}{\partial y} \quad w \right\}^{\mathrm{t}} = \mathbf{B}_{\boldsymbol{\eta}}\boldsymbol{\psi} \tag{15}$$

where

$$\mathbf{B}_{\boldsymbol{\eta}} = \left\{ \frac{\partial \boldsymbol{\Gamma}}{\partial x} \quad \frac{\partial \boldsymbol{\Gamma}}{\partial y} \quad \boldsymbol{\Gamma} \right\}^{\mathrm{t}} \tag{16}$$

Similarly, the vector of curvatures can be expressed as

$$\left\{ \frac{\partial^2 w}{\partial x^2} \quad \frac{\partial^2 w}{\partial y^2} \quad 2\frac{\partial^2 w}{\partial x\,\partial y} \right\}^{\mathrm{t}} = \mathbf{B}_{\boldsymbol{\kappa}}\boldsymbol{\psi} \tag{17}$$

where

$$\mathbf{B}_{\boldsymbol{\kappa}} = \left\{ \frac{\partial^2 \boldsymbol{\Gamma}}{\partial x^2} \quad \frac{\partial^2 \boldsymbol{\Gamma}}{\partial y^2} \quad 2\frac{\partial^2 \boldsymbol{\Gamma}}{\partial x\,\partial y} \right\}^{\mathrm{t}} \tag{18}$$

Here, both $\mathbf{B}_{\boldsymbol{\eta}}$ and $\mathbf{B}_{\boldsymbol{\kappa}}$ are 3×12 matrices.

The foregoing relations constitute the kinematics of the problem. The displacement components given by Eq. (6) and consequently the strain components described by Eq. (7) can be expressed as functions of nodal variables to be used in the Hamilton's principle given by Eq. (5).

Since the piezoceramic is poled in the thickness direction (z-direction), the non-zero electric field component (which is assumed to be uniform in the thickness direction) can be expressed as

$$E_z = -\frac{\partial \varphi}{\partial z} = -\frac{v_p}{h_p} \tag{19}$$

where the electric potential is assumed to be varying linearly across the electrode pair (i.e., the electric field is assumed to be uniform in the thickness direction). Then, the vector of electric field components becomes

$$\mathbf{E} = -\mathbf{B}_{\mathbf{E}} v_p \tag{20}$$

where

$$\mathbf{B}_{\mathbf{E}} = \left\{ 0 \quad 0 \quad \frac{1}{h_p} \right\}^{\mathrm{t}} \tag{21}$$

Based on the Hamilton's principle given by Eq. (5), the element mass matrix $\mathbf{m}$, stiffness matrix $\mathbf{k}$, electromechanical coupling vector $\boldsymbol{\theta}$, capacitance c_p and the mechanical forcing vector $\mathbf{f}$ can be expressed as

$$\mathbf{m} = \int_{V_s} \mathbf{B}_{\boldsymbol{\eta}}^t \mathbf{Z}^t \rho_s \mathbf{Z} \mathbf{B}_{\boldsymbol{\eta}} \, \mathrm{d}V_s + \int_{V_p} \mathbf{B}_{\boldsymbol{\eta}}^t \mathbf{Z}^t \rho_p \mathbf{Z} \mathbf{B}_{\boldsymbol{\eta}} \, \mathrm{d}V_p \tag{22a}$$

$$\mathbf{k} = \int_{V_s} z^2 \mathbf{B}_{\boldsymbol{\kappa}}^t \bar{\mathbf{c}}_s \mathbf{B}_{\boldsymbol{\kappa}} \, \mathrm{d}V_s + \int_{V_p} z^2 \mathbf{B}_{\boldsymbol{\kappa}}^t \bar{\mathbf{c}}_p^E \mathbf{B}_{\boldsymbol{\kappa}} \, \mathrm{d}V_p \tag{22b}$$

$$\boldsymbol{\theta} = \int_{V_p} z \mathbf{B}_{\boldsymbol{\kappa}}^t \bar{\mathbf{e}}^t \mathbf{B}_{\mathbf{E}} \, \mathrm{d}V_p \tag{22c}$$

$$c_p = \int_{V_p} \mathbf{B}_{\mathbf{E}}^t \bar{\boldsymbol{\varepsilon}}^S \mathbf{B}_{\mathbf{E}} \, \mathrm{d}V_p \tag{22d}$$

$$\mathbf{f} = \int_S \boldsymbol{\Gamma}^t f_w \, \mathrm{d}S \tag{22e}$$

where

$$\mathbf{Z} = \begin{bmatrix} -z & 0 & 0 \\ 0 & -z & 0 \\ 0 & 0 & 1 \end{bmatrix} \tag{23}$$

and an over-bar in Eqs. (22a)–(22e) respective term (stiffness, piezoelectric constant or permittivity) is defined in plane-stress conditions so that the formulation is in agreement with the Kirchhoff assumption. It is worthwhile adding that the mass and stiffness matrices ($\mathbf{m}$ and $\mathbf{k}$ are 12×12 matrices, the electromechanical coupling ($\boldsymbol{\theta}$) and the mechanical forcing vector ($\mathbf{f}$) are 12×1 vectors and the capacitance term (c_p) is a scalar. Note that the mechanical damping matrix will be introduced to the system in the global coordinates. It should also be recalled that the z term in the respective integrals is measured from the reference surface of the plate in the thickness direction [24,42].

As mentioned previously, in general, the source of excitation in energy harvesting from cantilevered plates is the motion of the clamped end. As discussed in the literature [23], if the base is vibrating in the transverse direction (z-direction), the effective force on the structure is due to the inertia of the structure in the same direction. Therefore, the forcing term in Eq. (22e) can be given by

$$f_w = -m^* a_B \tag{24}$$

where m^* is the mass per unit area of the finite element (including both the piezoceramic and the substructure layers) and a_B is the base acceleration. Here, it is assumed that both layers (piezoceramic and substructure) have the same mesh and the nodes are coincident.

The plane-stress form of the constitutive equations for the piezoelectric layer can be expressed as

$$\begin{Bmatrix} T_1 \\ T_2 \\ T_6 \\ D_3 \end{Bmatrix} = \begin{bmatrix} \bar{c}_{11}^E & \bar{c}_{12}^E & 0 & -\bar{e}_{31} \\ \bar{c}_{12}^E & \bar{c}_{22}^E & 0 & -\bar{e}_{32} \\ 0 & 0 & \bar{c}_{66}^E & 0 \\ \bar{e}_{31} & \bar{e}_{32} & 0 & \bar{\varepsilon}_{33}^S \end{bmatrix} \begin{Bmatrix} S_1 \\ S_2 \\ S_6 \\ E_3 \end{Bmatrix} \tag{25}$$

which is the reduced (2-D) form of Eq. (4b). Note that the elastic, piezoelectric and dielectric components in Eq. (25) are given in the contracted notation (i.e., Voigt's notation: 11→1, 22→2, 33→3, 23→4, 31→5 and 12→6) where 1, 2 and 3 directions are coincident with x, y and z directions.

In general, poled piezoelectric ceramics (e.g., PZT-5A, PZT-5 H) exhibit transversely isotropic material behavior (isotropic in the 12-plane, i.e., xy-plane) and therefore the plane-stress (2-D) components in Eq. (25) can be obtained in terms of the 3-D components as [43]

$$\bar{c}_{11}^E = c_{11}^E - \frac{(c_{13}^E)^2}{c_{33}^E}, \quad \bar{c}_{12}^E = c_{12}^E - \frac{c_{13}^E c_{23}^E}{c_{33}^E}, \quad \bar{c}_{22}^E = c_{22}^E - \frac{(c_{23}^E)^2}{c_{33}^E}, \quad \bar{c}_{66}^E = c_{66}^E$$

$$\bar{e}_{31} = e_{31} - \frac{c_{13}^E e_{33}}{c_{33}^E}, \quad \bar{e}_{32} = e_{32} - \frac{c_{23}^E e_{33}}{c_{33}^E}, \quad \bar{\varepsilon}_{33}^S = \varepsilon_{33}^S + \frac{e_{33}^2}{c_{33}^E} \tag{26}$$

Using these plane-stress forms of the elastic stiffness, piezoelectric and dielectric properties of the piezoceramic layer, the respective integrands of the piezoceramic layer in Eqs. (22a)–(22d) can be expressed as follows:

$$\mathbf{B}_{\boldsymbol{\eta}}^{\mathrm{t}} \mathbf{Z}^{\mathrm{t}} \rho_p \mathbf{Z} \mathbf{B}_{\boldsymbol{\eta}} = \rho_p \left[z^2 \frac{\partial \boldsymbol{\Gamma}^{\mathrm{t}}}{\partial x} \frac{\partial \boldsymbol{\Gamma}}{\partial x} + z^2 \frac{\partial \boldsymbol{\Gamma}^{\mathrm{t}}}{\partial y} \frac{\partial \boldsymbol{\Gamma}}{\partial y} + \boldsymbol{\Gamma}^{\mathrm{t}} \boldsymbol{\Gamma} \right] \tag{27a}$$

$$z^2 \mathbf{B}_{\boldsymbol{\kappa}}^{\mathrm{t}} \bar{\mathbf{c}}_p^E \mathbf{B}_{\boldsymbol{\kappa}} = z^2 \left[\bar{c}_{11}^E \frac{\partial^2 \boldsymbol{\Gamma}^{\mathrm{t}}}{\partial x^2} \frac{\partial^2 \boldsymbol{\Gamma}}{\partial x^2} + 2\bar{c}_{12}^E \frac{\partial^2 \boldsymbol{\Gamma}^{\mathrm{t}}}{\partial x^2} \frac{\partial^2 \boldsymbol{\Gamma}}{\partial y^2} + \bar{c}_{22}^E \frac{\partial^2 \boldsymbol{\Gamma}^{\mathrm{t}}}{\partial y^2} \frac{\partial^2 \boldsymbol{\Gamma}}{\partial y^2} + 4\bar{c}_{66}^E \frac{\partial^2 \boldsymbol{\Gamma}^{\mathrm{t}}}{\partial x \partial y} \frac{\partial^2 \boldsymbol{\Gamma}}{\partial x \partial y} \right] \tag{27b}$$

$$z \mathbf{B}_{\boldsymbol{\kappa}}^{\mathrm{t}} \bar{\mathbf{e}}^{\mathrm{t}} \mathbf{B}_{\mathrm{E}} = \frac{z}{h_p} \left(\bar{e}_{31} \frac{\partial^2 \boldsymbol{\Gamma}^{\mathrm{t}}}{\partial x^2} + \bar{e}_{32} \frac{\partial^2 \boldsymbol{\Gamma}^{\mathrm{t}}}{\partial x^2} \right) \tag{27c}$$

$$\mathbf{B}_{\mathbf{E}}^{\mathrm{t}} \bar{\boldsymbol{\varepsilon}}^S \mathbf{B}_{\mathbf{E}} = \frac{\bar{\varepsilon}_{33}^S}{h_p^2} \tag{27d}$$

For an isotropic substructure layer, the 2-D elastic stiffness matrix can be obtained for the plane-stress conditions as

$$\bar{\mathbf{c}}_s = \begin{bmatrix} 1 & \nu_s & 0 \\ \nu_s & 1 & 0 \\ 0 & 0 & \dfrac{1-\nu_s}{2} \end{bmatrix} \frac{Y_s}{1-\nu_s^2} \tag{28}$$

where ν_s is the Poisson's ratio and Y_s is the Young's modulus of the substructure material.

The global equations of motion are then obtained by assembling the element matrices given by Eqs. (22a)–(22e):

$$\mathbf{M}\ddot{\boldsymbol{\Psi}} + \mathbf{C}\dot{\boldsymbol{\Psi}} + \mathbf{K}\boldsymbol{\Psi} - \boldsymbol{\Theta}\mathbf{v} = \mathbf{F} \tag{29a}$$

$$\mathbf{C}_p\mathbf{v} + \mathbf{Q} + \boldsymbol{\Theta}^{\mathrm{t}}\boldsymbol{\Psi} = 0 \tag{29b}$$

where $\mathbf{M}$ is the global mass matrix ($n_m \times n_m$), $\mathbf{K}$ is the global stiffness matrix ($n_m \times n_m$) and $\boldsymbol{\Theta}$ are the global electromechanical coupling matrix ($n_m \times n_e$), $\mathbf{C}_p$ is the diagonal global capacitance matrix ($n_e \times n_e$), $\mathbf{F}$ is the global vector of mechanical forces ($n_m \times 1$), $\mathbf{Q}$ is the global vector of electric charge outputs ($n_e \times 1$), $\boldsymbol{\Psi}$ is the global vector of mechanical coordinates ($n_m \times 1$) and $\mathbf{v}$ is the global vector of voltage outputs ($n_e \times 1$). Here, n_m and n_e, respectively, are the number of mechanical and electrical degrees of freedom of the harvester plate. In Eq. (29a), the global mechanical damping matrix ($n_m \times n_m$) is assumed to be proportional to the mass and stiffness matrices:

$$\mathbf{C} = \alpha\mathbf{M} + \beta\mathbf{K} \tag{30}$$

where α and β are the constant of proportionality.

Since the number of electrical degrees of freedom is equal to the number of elements, the dimension of the global vector of voltage outputs in Eqs. (29a) and (29b) is equal to number of finite elements used in the mesh of the piezoceramic layer (n_e). This is a general case which assumes that each electromechanical finite element has its own electrode pair, insulated from one another. Thus, n_e number of different voltage outputs can be extracted from the system as Eq. (29b) represents n_e equations. In practice, however, piezoceramics come from the manufacturer with thin and very conductive electrode layers on the top and bottom surfaces. It is therefore reasonable to assume that all finite elements (n_e) generate the same voltage output so that the elements of vector $\mathbf{v}$ are identical (i.e., $v_1 = v_2 = \cdots v_{n_e} = v_p$) such that

$$\mathbf{v} = \{v_1 \;\; v_2 \ldots v_{n_e}\}^{\mathrm{t}} = \{1 \;\; 1 \ldots 1\}^{\mathrm{t}} v_p \tag{31}$$

This transformation takes into account the presence of full electrodes covering the top and the bottom surfaces of the piezoceramic of the unimorph (Fig. 1) and the potential difference between these two electrodes is simply v_p.

After defining the electromechanical coupling vector based on the transformation given by Eq. (31) as $\tilde{\boldsymbol{\Theta}} = \{1 \;\; 1 \ldots 1\}^{\mathrm{t}}\boldsymbol{\Theta}$ (which is a $n_m \times 1$ vector), taking the time derivative of Eq. (29b) and pre-multiplying by the $1 \times n_e$ vector $\{1 \;\; 1 \ldots 1\}$, one can obtain the following scalar equation:

$$C_p\dot{v}_p + \dot{Q} + \tilde{\boldsymbol{\Theta}}^{\mathrm{t}}\dot{\boldsymbol{\Psi}} = 0 \tag{32}$$

where $C_p = \mathrm{trace}(\mathbf{C}_p)$.

Since the electrical boundary condition due to a resistive load (R_l) is $\dot{Q} = v_p/R_l$, Eqs. (29a) and (32) become

$$\mathbf{M}\ddot{\boldsymbol{\Psi}} + \mathbf{C}\dot{\boldsymbol{\Psi}} + \mathbf{K}\boldsymbol{\Psi} - \tilde{\boldsymbol{\Theta}}v_p = \mathbf{F} \tag{33a}$$

$$C_p\dot{v}_p + \frac{v_p}{R_l} + \tilde{\boldsymbol{\Theta}}^{\mathrm{t}}\dot{\boldsymbol{\Psi}} = 0 \tag{33b}$$

which are the governing electromechanical equations for a unimorph piezoelectric energy harvester plate (Fig. 1).

If a bimorph piezoelectric energy harvester plate is considered (i.e., the substructure is bracketed by two identical piezoceramic layers) the mass, stiffness and consequently damping matrices are modified accordingly. It is known from the literature [44,25] that the electrode pairs covering each piezoceramic layer can be connected in series or in parallel to the external electrical load (for larger voltage or current, respectively). In general, the piezoceramic layers are poled in the same direction for parallel connection whereas they are poled in the opposite direction for series connection. For the parallel connection case, the effective electromechanical coupling vector is the sum of the individual contribution of each layer and the effective capacitance is the sum of each individual capacitances. For the series connection case, the effective electromechanical coupling vector is equal to that of one piezoceramic layer and the effective capacitance is one half of the capacitance of one piezoceramic layer.

3. Case studies

This section presents three case studies using the electromechanical FE model described in Section 2. In the first case study, the FE model is verified against the analytical results from the closed-form solution given by Erturk and Inman [24] for a unimorph harvester under base excitation. The second case study aims to predict the analytical and experimental

results for a bimorph harvester with a tip mass presented by Erturk and Inman [25]. The results for these two case studies are briefly discussed here and the details can be found in the respective papers [24,25]. After validating the electromechanical FE model, power optimization for a UAV wing spar with embedded piezoceramics is studied. The goal in this last case study is to find the geometric parameters (length and thickness) of the piezoceramic layers that give the maximum electrical power output under an imposed mass addition constraint.

The material and electromechanical properties for PZT-5A (used in all cases) are given in Table 1. It is worthwhile mentioning that manufacturers typically provide limited number of properties for piezoelectric ceramics. For instance, in the predictions of their analytical model, Erturk and Inman [25] used the data provided by Piezo Systems Inc. [45] as the data provided by the manufacturer was sufficient for a beam-type formulation. However, the plate-type formulation given here requires more than what is provided in the manufacturer's data sheet (see, for instance, the properties required for the calculation of the plane-stress elastic, piezoelectric and dielectric components in Eq. (26)). Therefore, the 3-D properties of PZT-5A [46] displayed in Table 1 are used here.

3.1. Verification against the analytical results for a unimorph configuration

The numerical input data of the unimorph studied by Erturk and Inman [24] is shown in Table 2. The results of the FE model are compared against the analytical solution in this section. The piezoceramic layer uniformly covers the substructure layer and the conductive electrodes are connected to a resistive electrical load as depicted in Fig. 1. Expressions for electromechanical FRFs, namely the voltage across the resistive load, current passing through the resistive load, electrical power output and relative tip motion, are obtained from the equations of motion defined in the FE model (Eqs. (33a) and (33b)). The electrical power FRF (per base acceleration) and the mechanical vibration FRF (relative tip displacement per base displacement) are presented in the following. The material, electromechanical and geometric properties given in Tables 1 and 2 are used in the FE simulations.

The excitation is due to the harmonic motion of the base in the transverse direction, $w_B(t) = Y_0 e^{j\omega t}$ (where $w_B(t)$ is the base displacement, Y_0 is its amplitude, ω is the excitation frequency and j is the unit imaginary number). At steady state, the voltage output-to-base acceleration FRF can be obtained from Eqs. (33a) and (33b) as

$$\frac{v_p(t)}{a_B(t)} = \frac{v_p(t)}{-\omega^2 Y_0 e^{j\omega t}} = j\omega\left(\frac{1}{R_l} + j\omega C_p\right)^{-1} \tilde{\boldsymbol{\Theta}}^{t}\left(-\omega^2\mathbf{M} + j\omega\mathbf{C} + \mathbf{K} + j\omega\left(\frac{1}{R_l} + j\omega C_p\right)^{-1}\tilde{\boldsymbol{\Theta}}\tilde{\boldsymbol{\Theta}}^{t}\right)^{-1}\mathbf{m}^{*} \tag{34}$$

where $\mathbf{m}^{*}$ is an $(n_m \times 1)$ mass vector obtained from the global forcing term $\mathbf{F}$ for the base excitation problem.

The electric current FRF is obtained by dividing the voltage FRF to the load resistance of the energy harvesting circuit. The electrical power FRF is the product of voltage and current FRFs and it is defined as the ratio of electrical power output to square of the base acceleration. Note that the modulus form of Eq. (34) is the peak voltage FRF (not the root mean square value). Therefore the electrical power obtained from this voltage FRF is the peak power and the average power amplitude is half of the peak power. The moduli of the power FRFs obtained from the FE model (thinner lines) for five

Table 1
Material and electromechanical properties of PZT-5A.

Mass density of the PZT (kg/m^3)	7800
Permittivity (nF/m)	$1800 \times \varepsilon_0$
c_{11}^E, c_{22}^E (GPa)	120.3
c_{12}^E (GPa)	75.2
c_{13}^E, c_{23}^E (GPa)	75.1
c_{33}^E (GPa)	110.9
c_{66}^E (GPa)	22.7
e_{31}, e_{32} (C/m^2)	−5.2
e_{33} (C/m^2)	15.9

Table 2
Geometric and material properties of the unimorph harvester.

Length of the beam (mm)	100
Width of the beam (mm)	20
Thickness of the substructure (mm)	0.5
Thickness of the PZT (mm)	0.4
Young's modulus of the substructure (GPa)	100
Mass density of the substructure (kg/m^3)	7165
Proportional constant—α (rad/s)	4.886
Proportional constant—β (s/rad)	1.2433×10^{-5}

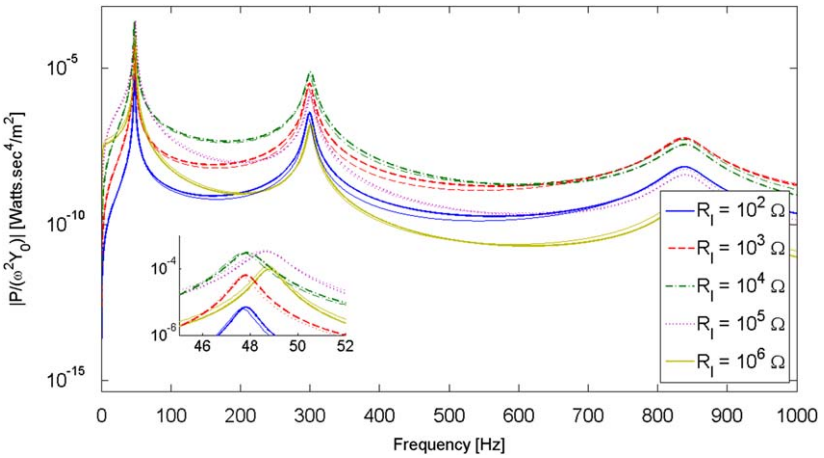

Fig. 3. Power FRFs for five different values of load resistance with the enlarged view of mode 1.

different values of load resistance are plotted in Fig. 3. These FRFs are in good agreement with the analytically obtained [24] curves (thicker lines).

The voltage FRF has a monotonic behavior with increasing load resistance for every excitation frequency. That is, the voltage across the resistive load increases with increasing load resistance and the frequency of maximum voltage output moves from short circuit to open circuit resonance frequency. The electrical current FRF exhibits an opposite behavior since current passing through the electrical load decreases with increasing load resistance for every excitation frequency [24]. The product of these two FRFs gives the electrical power, which shows intersections between the curves of different electrical loads (Fig. 3). That is, at a fixed frequency, the variation of peak power output with load resistance is not monotonic as can be seen from the enlarged view of the first mode plotted in Fig. 3. Consequently the short circuit resonance frequency (47.8 Hz) and the open circuit resonance frequency (48.8 Hz) have considerably different optimum load values [24] although the difference between these two frequencies is just 1 Hz. The short circuit and the open circuit resonance frequencies predicted by the FE model are 47.7 and 48.8 Hz, respectively.

The relative tip motion FRF is defined as the ratio of the amplitude of the displacement at the tip of the beam (relative to the base) to the amplitude of base displacement input and its is obtained from Eqs. (33a) and (33b) as

$$\frac{\mathbf{w}_{\mathrm{rel}}}{Y_0 \mathrm{e}^{\mathrm{j}\omega t}} = \omega^2 \left(-\omega^2 \mathbf{M} + \mathrm{j}\omega \mathbf{C} + \mathbf{K} + \mathrm{j}\omega \left(\frac{1}{R_l} + \mathrm{j}\omega C_p \right)^{-1} \tilde{\boldsymbol{\Theta}} \tilde{\boldsymbol{\Theta}}^{\mathrm{t}} \right)^{-1} \mathbf{m}^* \tag{35}$$

which defines a vector for the vibration response of all coordinates. Here, the component of interest in the vector defined by Eq. (35) is the transverse tip displacement.

The mechanical vibration (motion transmissibility) FRFs of the unimorph obtained from the FE model and the analytical solution are presented in Fig. 4. As can be observed from the enlarged view of Fig. 4, the vibration amplitude at short circuit resonance frequency (47.8 Hz) decreases as the load resistance is increased from 10^2 to $10^5\,\Omega$ due to the resistive shunt damping effect associated with power generation. The motion at the open circuit resonance frequency (48.8 Hz) is amplified with increasing load resistance. Simultaneous investigation of the enlarged views in Figs. 3 and 4 provides a better understanding of the piezoelectric shunt damping effect [47] with changing load resistance. The uncoupled FRF presented in Fig. 4 is the typical mechanical FRF (transmissibility) when no electromechanical coupling is considered. The electromechanically coupled vibration FRF converges to the uncoupled FRF when the system is close to short circuit conditions ($R_l \to 0$). Note that the inaccuracy in the FE predictions around the anti-resonance in Fig. 4 is related to the FE mesh size (25×5 finite elements for each layer in this case).

3.2. *Verification against the experimental and analytical results for a bimorph configuration*

In the second case study, the results obtained from the electromechanical FE model for a cantilevered bimorph with a tip mass under base excitation (Fig. 5) are compared with the single-mode analytical predictions of the closed-form solution and experimental results presented by Erturk and Inman [25]. The bimorph harvester configuration has a brass substructure bracketed by two PZT-5A layers. The piezoceramic layers are poled in the opposite directions and therefore the combination of the layers to the electrical load in Fig. 5 is the series connection case.

The expressions for the electromechanical FRFs are obtained from the global equations of motion. The voltage FRF has the same form of the expression for a unimorph harvester given by Eq. (34). However, the contribution of the additional piezoceramic layer has to be added to the mass, stiffness and damping matrices as well as to the mechanical forcing term. The tip mass also affects the mass matrix and the mechanical forcing term since the forcing vector is a function of the

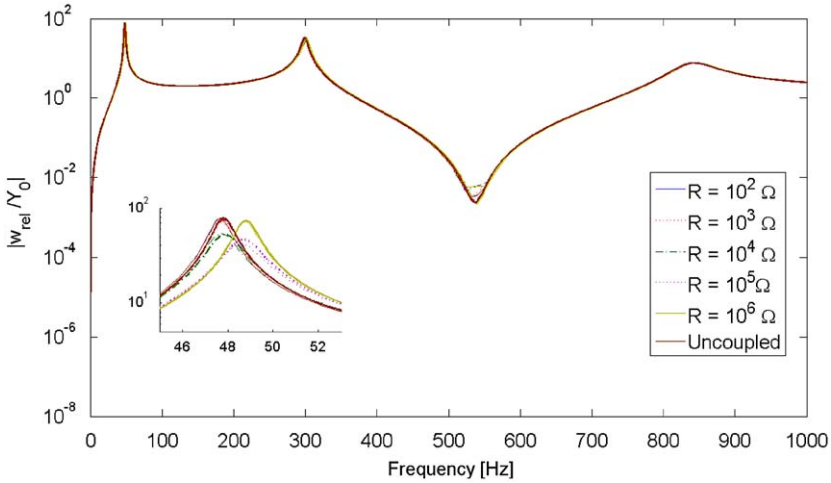

Fig. 4. Relative tip motion FRFs for five different values of load resistance with the enlarged view of mode 1.

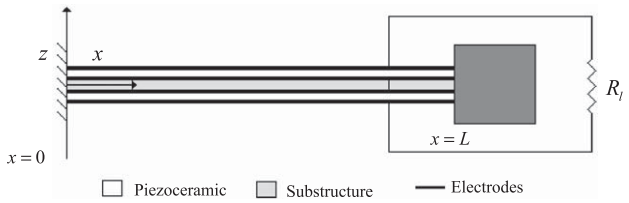

Fig. 5. Bimorph piezoelectric energy harvester (series connection).

Table 3
Geometric and material properties of the harvester.

Length of the beam (mm)	50.8
Width of the beam (mm)	31.8
Thickness of the substructure (mm)	0.14
Thickness of the PZT (mm)	0.26 (each)
Young's modulus of the substructure (GPa)	105
Mass density of the substructure (kg/m^3)	9000
Tip mass (kg)	0.012
Proportional constant—α (rad/s)	14.65
Proportional constant—β (s/rad)	10^{-5}

inertia of the structure in the base excitation problem. As stated previously, the effective piezoelectric coupling term in the series connection case is equal to the contribution of one piezoceramic layer and the effective capacitance is equal to one half of the contribution of one piezoceramic layer. The parameters used in the simulations are presented in Tables 1 and 3.

The voltage FRF is defined here as the voltage output per base acceleration (in terms of the gravitational acceleration, $g = 9.81\,\mathrm{m/s^2}$) to be in agreement with the experimental and analytical voltage FRFs given by Erturk and Inman [25]. Eq. (34), adapted to represent the bimorph harvester with a tip mass, is also easily modified to give voltage output per base acceleration. The voltage FRFs for the first mode of this harvester obtained from the FE model are plotted in Fig. 6 (12×8 finite elements were used for each layer in this case) along with the analytical solution and experimental results for eight different values of load resistance (1, 6.7, 11.8, 22, 33, 47, 100, 470 kΩ). A similar monotonic behavior of voltage output with increasing load resistance is observed for all excitation frequencies according to the numerical (FE model), analytical and experimental results. The experimental short circuit and open circuit resonance frequencies for the harvester are 45.6 and 48.4 Hz, respectively. The analytical model predicts these frequencies as 45.7 and 48.2 Hz, respectively. The FE model predictions of the short circuit and open circuit resonance frequencies are 45.7 and 48.3 Hz, respectively.

The mechanical vibration FRFs of the bimorph piezoelectric energy harvester obtained from the FE model, analytical model and experimental tests are presented in Fig. 7. The tip velocity FRF is defined as the ratio of the amplitude of velocity at the tip of the beam (relative to the fixed frame) to the gravitational acceleration as it is measured by a laser vibrometer located on the fixed ground. This FRF is easily obtained from the expression of the relative tip motion FRF

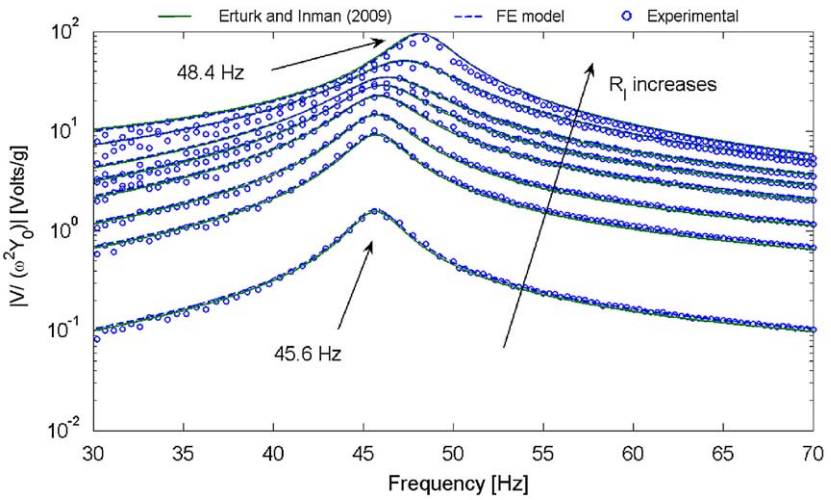

Fig. 6. Analytical, FE and experimental voltage FRFs for eight different values of load resistance.

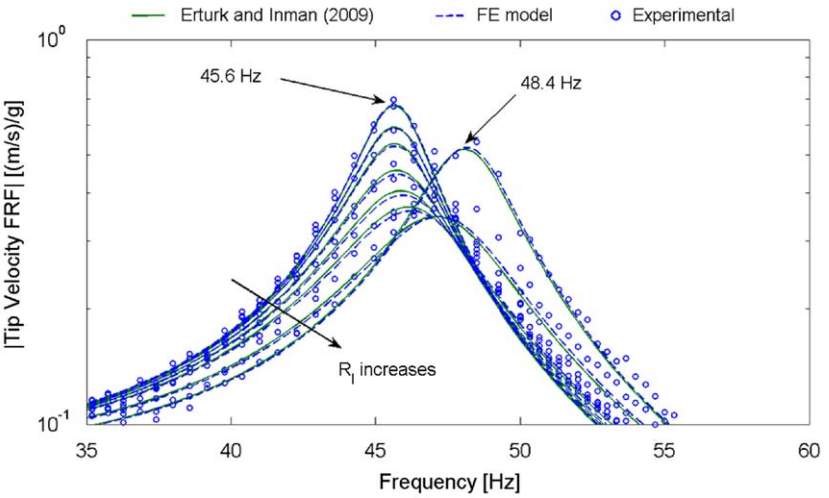

Fig. 7. Analytical, FE and experimental tip velocity FRFs for eight different values of load resistance.

(Eq. (35)) using $-jg/\omega(1+\mathbf{w}_{\mathrm{rel}}(L,t)/Y_0)$. It is observed in Fig. 7 that the mechanical FRFs obtained from the FE model are in agreement with the analytical and experimental results. The vibration amplitude at the short circuit resonance frequency is attenuated as the load resistance is increased up to 100 kΩ. Approximately after this value of load resistance, increasing load resistance amplifies the vibration amplitude at the open circuit resonance frequency and the vibration amplitude at the short circuit resonance frequency is no longer attenuated.

3.3. Design of an energy harvesting wing spar with embedded piezoceramics

Using the electromechanical FE model, an optimization problem is addressed in this section to design a UAV wing spar with embedded piezoceramics. This class of aircrafts has limited source of energy, limited size and load capacity. The generator spar, an additional source of energy with acceptable mass addition, could assist the general goal of maximum endurance and flight range or power small electronics components of the UAV.

The dimensions of the original wing spar are given as $300\times30\times12\,\mathrm{mm}^3$ and the purpose is to replace some part of the original spar material (aircraft aluminum alloy Al 2024-T3) by piezoceramic material (PZT-5A). Two identical layers of PZT-5A are embedded to the top and the bottom of the spar by replacing the original material as shown in Fig. 8. As the mass density of PZT-5A ($7800\,\mathrm{kg/m}^3$) is considerably larger than that of the aluminum alloy ($2750\,\mathrm{kg/m}^3$), the critical parameter in the optimization problem is the amount of mass added to the wing spar. Therefore, the following constraint is imposed

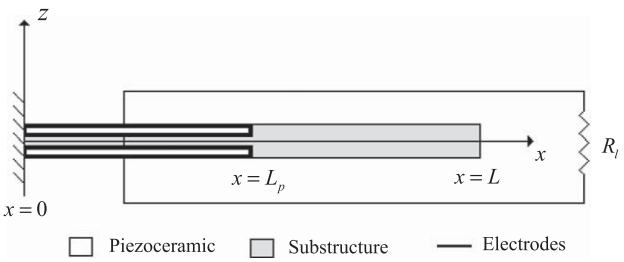

Fig. 8. Generator wing spar with embedded piezoceramics (series connection).

Table 4
Geometric and material properties of the aluminum wing spar.

Length of the spar (mm)	300
Width of the spar (mm)	30
Thickness of the spar (mm)	12
Young's modulus of the spar (GPa)	70.0
Mass density of the substructure (kg/m^3)	2750
Proportional constant—α (rad/s)	21.28
Proportional constant—β (s/rad)	10^{-5}

to the optimization problem: *The total mass added by the piezoceramic layers to the final configuration of the piezoelectric energy harvester wing spar should not exceed* 10% *of the mass of the original aluminum spar*. The goal is to find the optimal geometric configuration (length and thickness) of the embedded piezoceramic layers that will give the maximum electrical power output and satisfy the imposed mass restriction. The width of the piezoceramic is assumed to be the same as that of the spar.

It is worthwhile to mention that the following analysis assumes that the excitation amplitude (in terms of base acceleration of the spar, a_B) is not large enough to cause failure in the wing spar both for the original and the modified configurations. It is well known that typical piezoelectric ceramics are very brittle compared to classical engineering materials (such as the aircraft aluminum alloy considered here which has an ultimate tensile strength of 483 MPa according to Ref. [48]). Although the compressive strength values of piezoceramics are fairly large (Morganelectroceramics [49] reports the compressive strength of PZT-5A to be larger than 517 MPa), both the static and dynamic tensile strengths of PZT-5A are poor compared to typical engineering materials. The reported [49] static and dynamic tensile strength values of PZT-5A are 75.8 and 27.6 MPa, respectively. Therefore, clearly the original wing spar (made of Al 2024-T3) can carry larger base accelerations compared to the generator wing spar (Fig. 8). However, the following analysis provides the results normalized per base acceleration input, which is assumed to be smaller than the acceleration that would cause failure in the generator spar.

The geometric and material properties of the original spar (aircraft aluminum alloy Al 2024-T3) are presented in Table 4 (the properties of PZT-5A can be found in Table 1). The length-to-thickness ratio of the spar is slender enough to neglect the shear deformation and rotary inertia effects for the fundamental vibration mode. The source of excitation is assumed to be base excitation and the spar is assumed to have clamped-free boundary conditions, where the clamped end is the fuselage side of the spar. The oppositely poled piezoceramic layers are completely covered by conductive electrodes and combined in series.

The electromechanical behavior of the generator spar is initially investigated using a set of dimensions for two identical piezoceramic layers (Fig. 9). The length of the piezoceramic layers is increased with a fixed increment (10% of the spar length). At each length, the electromechanical behavior is investigated for eleven different thickness values of the layers, ranging from 0.3 to 3.3 mm with an increment of 0.3 mm. For each geometric configuration, the electromechanical system is assumed to be excited at the short circuit resonance frequency of the first vibration mode. Thus, the power output, the parameter to be optimized within the boundaries established by the mass restriction, is obtained for a wide range of load resistance until the optimal one is observed. Variation of the maximum electrical power output with dimensionless length and dimensionless thickness of the piezoelectric energy harvester is displayed in Fig. 9a (75×8 finite elements were used for each layer in this case). The dimensionless length (L^*) is defined as the length of the piezoceramic layers (L_p) divided by the total length of the spar (L) whereas the dimensionless height (h^*) is the height of one piezoceramic layer (h_p) divided by the total height of the spar (i.e., $L^* = L_p/L$ and $h^* = h_p/h$). It should be noted that the optimum electrical load that corresponds to each data point in Fig. 9a is different (Fig. 9b).

Fig. 10 shows the top view of Fig. 9a along with the *limiting solution* that satisfies the mass restriction. It is straightforward to show that the mass restriction implies $L^* \times h^* \leq 0.027225$. Therefore, the hyperbola that defines the limiting solution in Fig. 9b is the curve $L^* = 0.027225/h^*$. The combinations (L^*, h^*) above this curve exceed the given mass

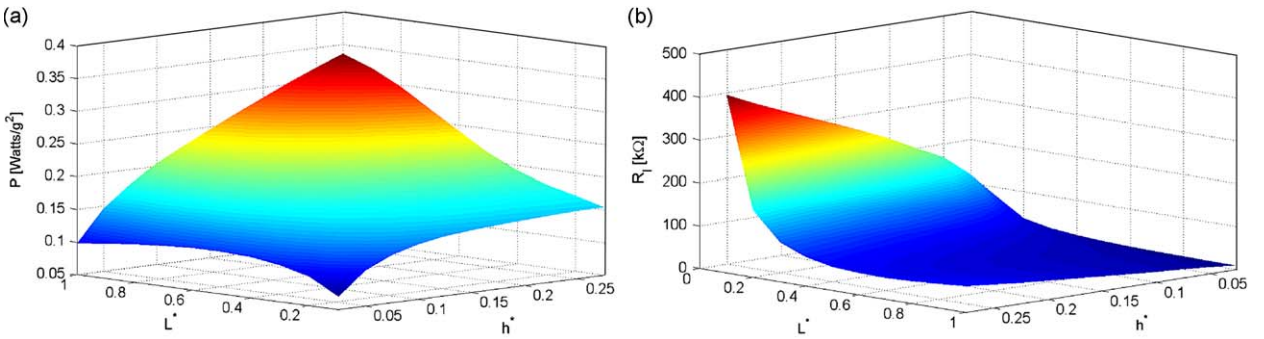

Fig. 9. Variation of the (a) maximum power output and (b) optimum load resistance with the dimensionless length and dimensionless thickness of the piezoceramic layers.

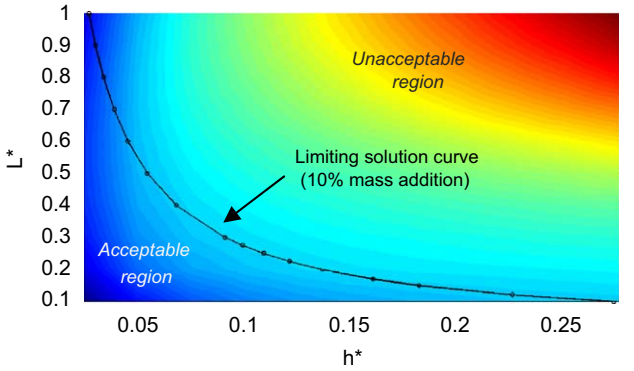

Fig. 10. Variation of the power output with the dimensionless length and dimensionless thickness of the piezoceramic layers: top view of Fig. 9a with the limiting solution curve.

addition limit (10% of the original spar mass) whereas those below the curve satisfy the given condition. The problem is then to find the optimal solution on the limiting curve. Before that, it is useful to discuss the trends in Fig. 9a.

As the plane-stress elastic stiffnesses (Young's moduli) of the aluminum alloy and PZT-5A are similar, the bending stiffness of any configuration of the generator spar (any length and thickness) is similar to that of the original aluminum spar (since the cross section is always the same). However, as the mass density of the piezoceramic is much larger than that of aluminum, the mass of any configuration of the generator spar is larger than that of the original spar. Since the source of mechanical forcing in the base excitation problem is the inertia of the body itself, the problem analyzed here is more related to variation of inertia (in terms of amount of added mass and its distribution) than that of stiffness. Furthermore, since one is interested in the resonance behavior, variation of mechanical damping is also important. It can be recalled from Eq. (30) that the mechanical damping is assumed to be proportional to the stiffness and mass matrices. However, the damping ratio in this case study is affected mainly from mass variation since the stiffness of the structure is not changed considerably. That is, increased mass results in increased mechanical damping as the stiffness is not decreased. The interesting trade-off in terms of the power output is between the excitation amplitude and the mechanical damping, since mass addition increases both. Although increased excitation amplitude implies increased power, expectedly, increased mechanical damping has the opposite effect.

As can be observed from Fig. 9a, the power output increases with increasing dimensionless thickness for any dimensionless length. One could expect the opposite behavior of power output with increasing thickness based on the fact that the electromechanical coupling (or piezoelectric coupling matrix in the FE model) is directly proportional to the distance from the mid-surface of piezoceramic layer to the reference surface of the composite structure. However, increased thickness of the piezoceramic layers also means increased inertia of the elastic body and consequently larger mechanical forcing in the base excitation problem. Moreover the dynamic flexibility of the generator spar is increased as can be observed by analyzing the behavior of the short circuit natural frequency with dimensionless length and thickness plotted in Fig. 11a (note that the length and thickness axes are reversed for clarity). As the case analyzed here is much more related to mass variation than stiffness variation, natural frequencies are reduced with increasing dimensions of the piezoceramic layers. It can be observed from Fig. 11a that the lowest natural frequency (72.8 Hz) is obtained for maximum length and thickness whereas the highest natural frequency (109.1 Hz) is obtained for the minimum dimensions of the piezoceramic layer. As a consequence, larger strains and larger power outputs are observed with increasing dimensionless

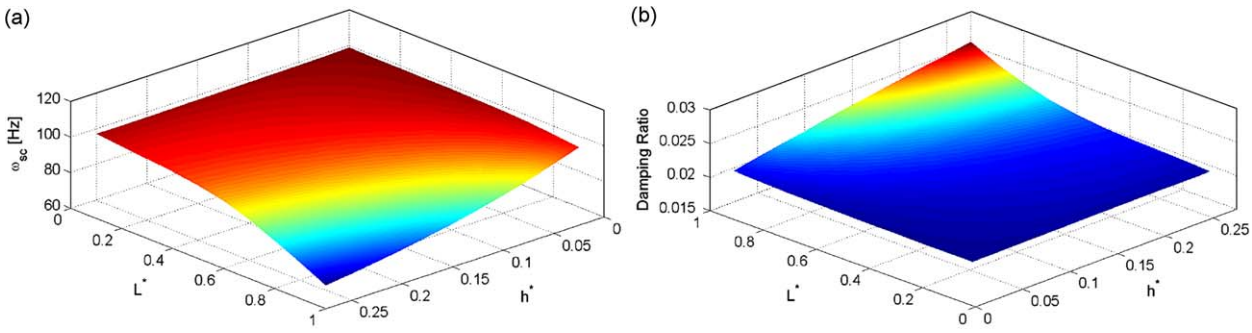

Fig. 11. Variation of the (a) short circuit resonance frequency and the (b) mechanical damping ratio with dimensionless length and thickness of the piezoceramic layers (for the fundamental vibration mode).

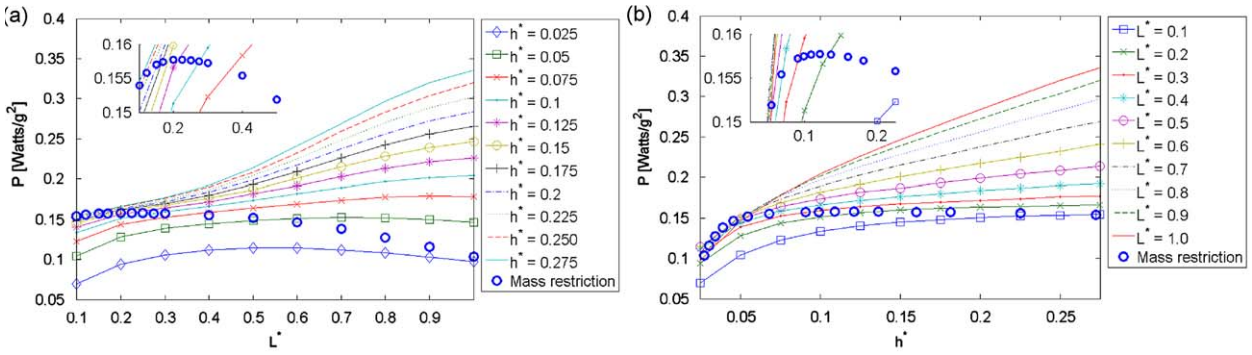

Fig. 12. (a) Power output versus dimensionless length for a range of dimensionless thickness and (b) power output versus dimensionless thickness for a range of dimensionless length (with the limiting solution).

thickness. Thus, the favorable effect of increased inertia (which constitutes the mechanical forcing in the base excitation problem) and flexibility overcomes the negative effect of reduced distance from the mid-surface of piezoceramic layer to the reference surface and the negative effect of increased damping (Fig. 11b). It should be noted that this behavior is amplified for larger values of dimensionless length.

Fig. 12a and b, respectively, show the side views of Fig. 9a along with the limiting solution (the curve in Fig. 10) that gives 10% mass addition. One can therefore analyze the behavior of power output with increasing dimensionless length for fixed values of dimensionless thickness in Fig. 12a. It is useful to consider two different thickness sets separately in Fig. 12a: the first one is for dimensionless thicknesses from 0.02 to 0.075 and the second one is from 0.075 to 0.275. For the first set of data curves (thin piezoceramics) a peak value of power output is observed with increasing length. Considering the strain distribution for a cantilevered beam, a peak value for the power versus length of piezoceramic is not expected for a fixed thickness. It turns out that, for thin piezoceramics with approximately $L^* > 0.5$, the effect of increased mass and consequently increased mechanical forcing and increased dynamic flexibility (due to reduced natural frequency) cannot overcome the negative effect of increased damping which is also due to increased mass and which reduces the amplitude of vibration and the electrical output. The variation of damping ratio with dimensionless length and thickness can be referred from Fig. 11b. A simple verification was performed by the authors considering damping to be proportional to stiffness only (which is similar to assuming constant damping for every configuration since the elastic stiffnesses of piezoceramics and aluminum are similar). In this case, expectedly, a maximum value for the electrical power is not observed with increasing length for a fixed thickness. For the set of curves with thicker piezoceramics in Fig. 12a, it is clear that the maximum value of power output gets closer to the free end of the generator spar. For the maximum thickness considered here, the maximum power is observed for $L^* = 1.0$. Once again, the general behavior is related to the amount of mass added, mechanical forcing term, structural dynamic flexibility (in the sense of reduced natural frequency) and mechanical damping. Increased excitation due to thicker piezoceramic overcomes the negative effect of damping on the mechanical and consequently the electrical response amplitudes. One can conclude that the mass added in the region around the free end of the spar has an effect similar to that of a tip mass on the general behavior of the generator spar. The limiting solution is also given in Fig. 12b along with the curves of fixed length. The power outputs increases monotonically with increasing thickness for each length of embedded piezoceramic.

If no mass restriction was imposed to the problem, the configuration with maximum length and thickness would be the best one in terms of energy harvesting. However, the main goal here is to optimize the power output and satisfy the mass

Table 5
Limiting solutions for the mass restriction problem.

L^*	h^*	P (mW/g^2)	R (kΩ)	ω_{sc} (Hz)
0.1	0.27225	154.00	410	107.36
0.15	0.18150	156.98	107	107.05
0.2	0.36166	157.69	104	106.97
0.225	0.12100	157.72	84	106.97
0.25	0.10892	157.65	70	106.98
0.275	0.98999	157.48	60	107.00
0.3	0.09075	157.23	51	107.03
0.4	0.06807	155.38	32	107.10
0.5	0.05446	151.91	23	107.04
0.6	0.04538	146.27	18	106.79
0.7	0.03890	138.10	14	106.29
0.8	0.03403	127.56	12	105.55
0.9	0.03025	115.50	10	104.56
1.0	0.02723	103.22	8.5	103.34

restriction constraint which requires $L^* \times h^* \leq 0.027225$. The limiting solution ($L^* \times h^* = 0.027225$) is seen in Fig. 10 from the top view and in Fig. 12a and b from the side views. Sample data points from the limiting solution are also listed in Table 5. The zoomed views in Fig. 12 allow reading the values of L^* and h^* that gives the maximum power for 10% mass addition as $L^* = 0.225$ and $h^* = 0.121$. That is, the optimum solution for the given design constraint is obtained when the two piezoceramic layers are embedded at the root covering 22.5% of the total length, each having a thickness that is 12.1% of the total thickness. From Table 4, for $L = 300$ mm and $h = 12$ mm, the length and the thickness of each embedded piezoceramic layer in Fig. 8 are obtained as $L_p = 67.5$mm and $h_p = 1.45$ mm, respectively. The electrical power per base acceleration for the generator spar is obtained as 157.72 mW/g^2.

4. Conclusions

In this paper, an electromechanical FE plate model is derived for piezoelectric energy harvesting from base excitations. The mechanics of the plate is based on the classical (Kirchhoff) plate theory, which is appropriate for modeling of typical piezoelectric energy harvesters since they are usually designed and manufactured as thin plates. The electromechanical FE model is derived based on generalized Hamilton's principle for electroelastic bodies and it accounts for the presence of a pair of conductive electrodes covering the entire piezoceramic layer. A resistive electrical load is considered in the electrical domain. Derivations are given for predicting the coupled mechanical vibration and electrical power response of the harvester plate due to base excitation.

The electromechanical model is first verified against the analytical results obtained from the closed-form solution for a unimorph cantilever under base excitation reported in the literature. The electromechanical vibration and power FRFs obtained from the FE model are in very good agreement with the ones obtained from the analytical solution. The second verification is presented for a bimorph cantilever with a tip mass under base excitation. It is shown that the electromechanical FE model can successfully predict the analytical and the experimental results of the bimorph reported in the literature.

UAVs constitute important application systems where generating electrical energy from waste vibration energy available during the flight has an important practical value. The electrical power generated from structural vibrations of a UAV can be used to power small electronic components of the UAV and ultimately to increase its flight time if possible. With this motivation, an optimization problem is investigated in the last case study to design a generator wing spar with embedded piezoceramics. Although the purpose is to obtain the maximum power output, mass addition is the greatest penalty in aerospace applications. Thus, the wing spar is modified by embedding piezoceramic into the spar by removing some of the original material. However, since piezoelectric ceramics are typically much heavier than aircraft materials (such as aluminum alloys), a design constraint is imposed for the added mass (not to exceed 10% of the original spar mass). The generator spar with embedded piezoceramics is considered as a bimorph configuration with two piezoceramic layers in series connection. It is shown that the maximum power for 10% mass addition to the spar is obtained when the two piezoceramic layers are embedded at the root covering 22.5% of the total length, each having a thickness that is 12.1% of the total thickness.

In the analysis given here for the UAV application, the source of mechanical forcing is assumed to be base excitation with no air flow to simplify the problem. The optimization problem investigated in this work becomes more realistic if an unsteady aerodynamic model is combined with the governing equations. In such a case, the effect of the aerodynamic damping alters the dynamic behavior of the wing during the flight. The presence of aeroelastic coupling in addition to piezoelectric coupling results in further variation of the natural frequencies, yielding different values for the electrical

power outputs as well as for the optimum values of load resistance. Combination of the piezoelectrically coupled FE model given here with an appropriate aeroelastic model is currently investigated by the authors.

Acknowledgments

The authors gratefully acknowledge the support of the Air Force Office of Scientific Research MURI under Grant number F 9550-06-1-0326 "Energy Harvesting and Storage Systems for Future Air Force Vehicles" monitored by Dr. B.L. Lee. The authors also gratefully acknowledge the support of CAPES (Brazil).

References

[1] H.A. Sodano, D.J. Inman, G. Park, A review of power harvesting from vibration using piezoelectric materials, *The Shock and Vibration Digest* 36 (2004) 197–205.
[2] S.P. Beeby, M.J. Tudor, N.M. White, Energy harvesting vibration sources for microsystems applications, *Measurement Science and Technology* 13 (2006) R175–R195.
[3] S. Priya, Advances in energy harvesting using low profile piezoelectric transducers, *Journal of Electroceramics* 19 (2007) 167–184.
[4] S.R. Anton, H.A. Sodano, A review of power harvesting using piezoelectric materials (2003–2006), *Smart Materials and Structures* 16 (2007) R1–R21.
[5] K.A. Cook-Chennault, N. Thambi, A.M. Sastry, Powering MEMS portable devices—a review of non-regenerative and regenerative power supply systems with emphasis on piezoelectric energy harvesting systems, *Smart Materials and Structures* 17 (2008) 043001 (33pp.).
[6] S.R. Anton, D.J. Inman, Vibration energy harvesting for unmanned air vehicles, *Smart Structures and Materials 2008*: *Active and Passive Smart Structures and Integrated Systems II*, *Proceedings of the SPIE*, Vol. 6928, San Diego, CA, March 10–13, 2008.
[7] K.C. Magoteaux, B. Sanders, H.A. Sodano, Investigation of energy harvesting small unmanned air vehicle, *Smart Structures and Materials 2008*: *Active and Passive Smart Structures and Integrated Systems II*, *Proceedings of the SPIE*, Vol. 6928, San Diego, CA, March 10–13, 2008.
[8] A. Erturk, J.M. Renno, D.J. Inman, Modeling of piezoelectric energy harvesting from an L-shaped beam-mass structure with an application to UAVs, *Journal of Intelligent Material Systems and Structures* 20 (2009) 529–544.
[9] S. Roundy, P.K. Wright, J. Rabaey, A study of low level vibrations as a power source for wireless sensor nodes, *Computer Communications* 26 (2003) 1131–1144.
[10] H.A. Sodano, G. Park, D.J. Inman, Estimation of electric charge output for piezoelectric energy harvesting, *Strain* 40 (2004) 49–58.
[11] N.E. duToit, B.L. Wardle, Experimental verification of models for microfabricated piezoelectric vibration energy harvesters, *AIAA Journal* 45 (2007) 1126–1137.
[12] A. Erturk, O. Bilgen, D.J. Inman, Power generation and shunt damping performance of a single crystal lead magnesium niobate–lead zirconate titanate unimorph: analysis and experiment, *Applied Physics Letters* 93 (2008) 224102 (3pp.).
[13] C.B. Williams, R.B. Yates, Analysis of a micro-electric generator for microsystems, *Sensors and Actuators A* 52 (1996) 8–11.
[14] D. Arnold, Review of microscale magnetic power generation, *IEEE Transactions on Magnetics* 43 (2007) 3940–3951.
[15] P. Glynne-Jones, M.J. Tudor, S.P. Beeby, N.M. White, An electromagnetic, vibration-powered generator for intelligent sensor systems, *Sensors and Actuators A* 110 (2004) 344–349.
[16] S.P. Beeby, R.N. Torah, M.J. Tudor, P. Glynne-Jones, T. O'Donnell, C.R. Saha, S. Roy, A micro electromagnetic generator for vibration energy harvesting, *Journal of Micro-electromechanical Engineering* 17 (2007) 1257–1265.
[17] B.P. Manna, N.D. Sims, Energy harvesting from the nonlinear oscillations of magnetic levitation, *Journal of Sound and Vibration* 319 (2009) 515–530.
[18] S. Roundy, P.K. Wright, J. Rabaey, Micro-electrostatic vibration-to-electricity converters, *Proceedings of the ASME 2002 International Mechanical Engineering Congress and Exposition*, 2002.
[19] P. Mitcheson, P. Miao, B. Start, E. Yeatman, A. Holmes, T. Green, MEMS electrostatic micro-power generator for low frequency operation, *Sensors and Actuators A* 115 (2004) 523–529.
[20] N.E. duToit, B.L. Wardle, S.-G. Kim, Design considerations for MEMS-scale piezoelectric mechanical vibration energy harvesters, *Integrated Ferroelectrics* 71 (2005) 121–160.
[21] S.-N. Chen, G.-J. Wang, M.-C. Chien, Analytical modeling of piezoelectric vibration-induced micro power generator, *Mechatronics* 16 (2006) 379–387.
[22] J.H. Lin, X.M. Wu, T.L. Ren, L.T. Liu, Modeling and simulation of piezoelectric MEMS energy harvesting device, *Integrated Ferroelectrics* 95 (2007) 128–141.
[23] A. Erturk, D.J. Inman, Issues in mathematical modeling of piezoelectric energy harvesters, *Smart Materials and Structures* 17 (2008) 065016 (14pp.).
[24] A. Erturk, D.J. Inman, A distributed parameter electromechanical model for cantilevered piezoelectric energy harvesters, *ASME Journal of Vibration and Acoustics* 130 (2008) 041002 (15pp.).
[25] A. Erturk, D.J. Inman, An experimentally validated bimorph cantilever model for piezoelectric energy harvesting from base excitations, *Smart Materials and Structures* 18 (2009) 025009.
[26] N. Elvin, A. Elvin, A general equivalent circuit model for piezoelectric generators, *Journal of Intelligent Material Systems and Structures* 20 (2009) 3–9.
[27] N.G. Stephen, On energy harvesting from ambient vibration, *Journal of Sound and Vibration* 293 (2006) 409–425.
[28] J.M. Renno, M.F. Daqaq, D.J. Inman, On the optimal energy harvesting from a vibration source, *Journal of Sound and Vibration* 320 (2009) 386–405.
[29] H.S. Tzou, C.I. Tseng, Distributed piezoelectric sensor/actuator design for dynamic measurement/control of distributed parameter systems: a piezoelectric finite element approach, *Journal of Sound and Vibration* 138 (1990) 17–34.
[30] W.S. Hwang, H.C. Park, Finite element modeling of piezoelectric sensors and actuators, *AIAA Journal* 31 (1993) 930–937.
[31] D.T. Detwiler, M.-H.H. Shen, V.B. Venkayya, Finite element analysis of laminated composite structures containing distributed piezoelectric actuators and sensors, *Finite Elements in Analysis and Design* 20 (1995) 87–100.
[32] S.H. Chen, Z.D. Wang, X.H. Liu, Active vibration control and suppression for intelligent structures, *Journal of Sound and Vibration* 200 (1997) 167–177.
[33] S.Y. Wang, A finite element model for the static and dynamic analysis of a piezoelectric bimorph, *International Journal of Solids and Structures* 41 (2004) 4075–4096.
[34] G.K. Ottman, H.F. Hofmann, A.C. Bhatt, G.A. Lesieutre, Adaptive piezoelectric energy harvesting circuit for wireless remote power supply, *IEEE Transactions on Power Electronics* 17 (2002) 669–676.
[35] D. Guyomar, A. Badel, E. Lefeuvre, Toward energy harvesting using active materials and conversion improvement by nonlinear processing, *IEEE Transactions on Ultrasonics, Ferroelectrics and Frequency Control* 52 (2005) 584–595.
[36] Y.C. Shu, I.C. Lien, Analysis of power output for piezoelectric energy harvesting systems, *Smart Materials and Structures* 15 (2006) 1499–1512.
[37] M.J. Guan, W.H. Liao, On the efficiencies of piezoelectric energy harvesting circuits towards storage device voltages, *Smart Materials and Structures* 16 (2007) 498–505.
[38] S.H. Crandall, D.C. Karnopp, E.F. Kurtz Jr., D.C. Pridmore-Brown, *Dynamics of Mechanical and Electromechanical Systems*, McGraw-Hill, New York, 1968.
[39] N.W. Hagood, W.H. Chung, A. Von Flotow, Modelling of piezoelectric actuator dynamics for active structural control, *Journal of Intelligent Material Systems and Structures* 1 (1990) 327–354.

[40] IEEE Group on Sonics and Ultrasonics, IEEE Standard on Piezoelectricity, New York, 1978.
[41] K.-J. Bathe, *Finite Element Procedures*, Prentice-Hall, Englewood Cliffs, NJ, 1996.
[42] F.P. Beer, E.R. Johnston Jr., *Mechanics of Materials*, McGraw-Hill, New York, 1992.
[43] A.A. Bent, Piezoelectric Fiber Composites for Structural Actuation, PhD Thesis, Massachusetts Institute of Technology, 1994.
[44] Q.M. Wang, L.E. Cross, Constitutive equations of symmetrical triple layer piezoelectric benders, *IEEE Transactions on Ultrasonics, Ferroelectrics, and Frequency Control* 46 (1999) 1343–1351.
[45] 〈http://www.piezo.com/prodsheet1sq5A.html〉, Accessed December 2008.
[46] 〈http://www.efunda.com/materials/piezo/material_data〉, Accessed December 2008.
[47] G.A. Lesieutre, G.K. Ottman, H.F. Hofmann, Damping as a result of piezoelectric energy harvesting, *Journal of Sound and Vibration* 269 (2004) 991–1001.
[48] 〈http://asm.matweb.com/〉, Accessed December 2008.
[49] 〈http://www.morganelectroceramics.com/〉, Accessed December 2008.